1	Interfacial Solar Evaporation by 3D Graphene Oxide Stalk for
2	Highly Concentrated Brine Treatment
3	
4	Research article
5	
6	Environmental Science & Technology
7	
8	Casey T.K. Finnerty, Akanksha K. Menon, Kelly M. Conway, Daryn
9	Lee, ¹ Matthew Nelson, ¹ Jeffrey J. Urban ³ , David Sedlak ¹ , and Baoxia Mi ¹ *
10	
11 12	¹ Department of Civil and Environmental Engineering, University of California, Berkeley, California 94720, United States
13 14	² Energy Storage and Distributed Resources Division, Lawrence Berkeley National Laboratory, Berkeley, California 94720, United States
15 16	³ The Molecular Foundry, Lawrence Berkeley National Laboratory, Berkeley, California 94720, United States
17	
18	*The author to whom correspondence should be addressed.
19	E-mail: mib@berkeley.edu
20	

Abstract

21

22

23

24

25

26

27

28

29

30

31

32

33

34

35

36

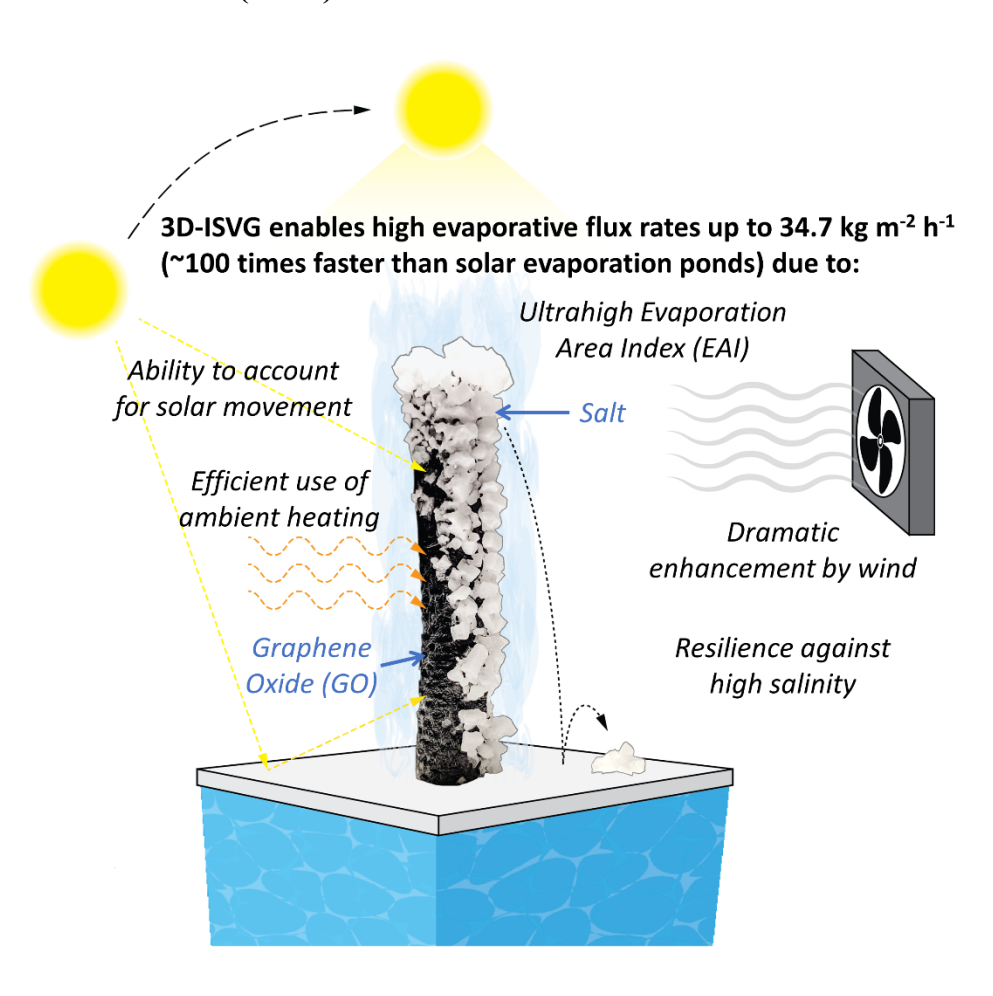
In this work, we demonstrate a 3-dimensional Graphene Oxide (3D GO) stalk that operates near the capillary wicking limit to achieve an evaporation flux of 34.7 kg m⁻² h⁻¹ under 1-sun condition (1 kW/m²). This flux represents nearly a 100 times enhancement over a conventional solar evaporation pond. Interfacial solar vapor generation traditionally uses 2D evaporators to vaporize water using sunlight, but their low evaporative water flux limits their practical applicability for desalination. Some recent studies using 3D evaporators demonstrate potential for more efficient water transfer, but the flux improvement has been marginal because of low evaporation area index (EAI), which is defined as the ratio of total evaporative surface area to projected ground area. By using a 3D GO stalk with an ultrahigh EAI of 70, we achieved nearly a twenty-fold enhancement over 2D GO evaporator. The 3D GO stalk also exhibited additional advantages including omnidirectional sunlight utilization, high evaporation flux under dark conditions from more efficient utilization of ambient heating, dramatic increase of evaporation rate by introducing wind, scaling resistance in evaporating brines with a salt content of up to 17.5 wt%. This performance makes the 3D GO stalk well-suited for the development of a low-cost, reduced footprint technology for zero liquid discharge in brine management applications.

37

38

- KEYWORDS: interfacial solar vapor generation, 3D evaporator, solar desalination, zero liquid
- 39 discharge, evaporation area index, graphene oxide
- 40 SYNOPSIS: This paper reported the performance of a 3D solar evaporator and its potential as a
- 41 sustainable brine treatment technology.

Table of Contents (TOC)



INTRODUCTION

Global water security is being threatened by rapidly increasing water demand, primarily driven by population growth. Concurrently, overexploitation, pollution, and climate change are decreasing the availability of traditional water resources, which is estimated to cause an additional 1.8 billion people to fall into water stress in the next 30 years. Expanding to alternative water supplies typically involves advanced treatment, often by reverse osmosis (RO). However, RO requires large capital investment, technical expertise, established supply chains, and a reliable supply of high-grade energy to operate. Furthermore, brine produced by RO has to be properly managed, which severely limits where RO can be affordably implemented, especially when ocean disposal is impractical.

Interfacial solar vapor generation is an emerging approach to sustainably desalinate water using sunlight, while being capable of achieving zero liquid discharge.^{6,7} In recent literature, interfacial solar evaporation is most often achieved using flat, two-dimensional (2D) materials that float at the air-water interface, where water is wicked into the material's porous structure, photothermally heated by sunlight, and efficiently evaporated.⁸ Although optimization of material properties, heat localization, and water replenishment rates have led to extremely high solar-vapor conversion efficiencies, evaporative fluxes from 2D evaporators are still low, typically between 1.5 to 3.0 kg m⁻² h⁻¹, ⁹⁻¹² which would result in a relatively large footprint.

Recently, researchers have proposed the use of 3D evaporators to increase the water production performance.¹³ As the name suggests, these 3D structures utilize capillary pumping to supply water to additional surfaces for evaporation.¹⁴ This enables 3D evaporator to achieve evaporation area index (EAI) values (ratio of total area available for evaporation relative to projected ground area) that are greater than 1. Figure 1A summarizes some 3D geometries that

have been reported in the literature, including hierarchical structures that contain microscopic 3D features to increase the EAI to around 1.2,^{15,16} curved and folded 2D sheets that lead to an increased EAI of around 1.5,^{17–19} 2D sheets that were intentionally converted into 3D geometries to obtain an EAI up to 3 by means of cutting and pasting,^{20–22} and more recently bio-inspired^{23–25} and other 3D evaporators^{26–28} structures that generally result in EAI values of 5 and higher. The evaporative water flux of these 3D evaporators were higher than most 2D counterparts, but they have remained less than 5 kg m⁻² h⁻¹, with only a few 3D evaporators achieving the higher EAI values^{29,30} that are needed to make this approach attractive in practice. Therefore, there is a need to develop an inexpensive, simple 3D evaporator that can achieve a substantially higher EAI that will result in the necessary improvement in water flux.

To address this challenge, we analyzed three geometries (i.e., dome, cone, and cylinder) through mathematical modeling to facilitate the design of 3D evaporators. After finding the optimal geometry being cylinder, we synthesized a cylindrical, 3D GO stalk that effectively absorbs solar light and takes full advantage of capillary pumping to achieve significant increases in EAI and evaporative surface area. We investigated this 3D design in comparison with a 2D system to evaluate the potential advantages of 3D evaporators, including water flux enhancement, omni-directional light absorption, utilization of wind-induced convection, and scaling resistance with high-salinity brine. These findings are especially relevant as research efforts transition from material synthesis to technology design, with the 3D GO stalk showing promise to reduce the spatial footprint of brine evaporation and potentially achieve zero-liquid-discharge (ZLD).

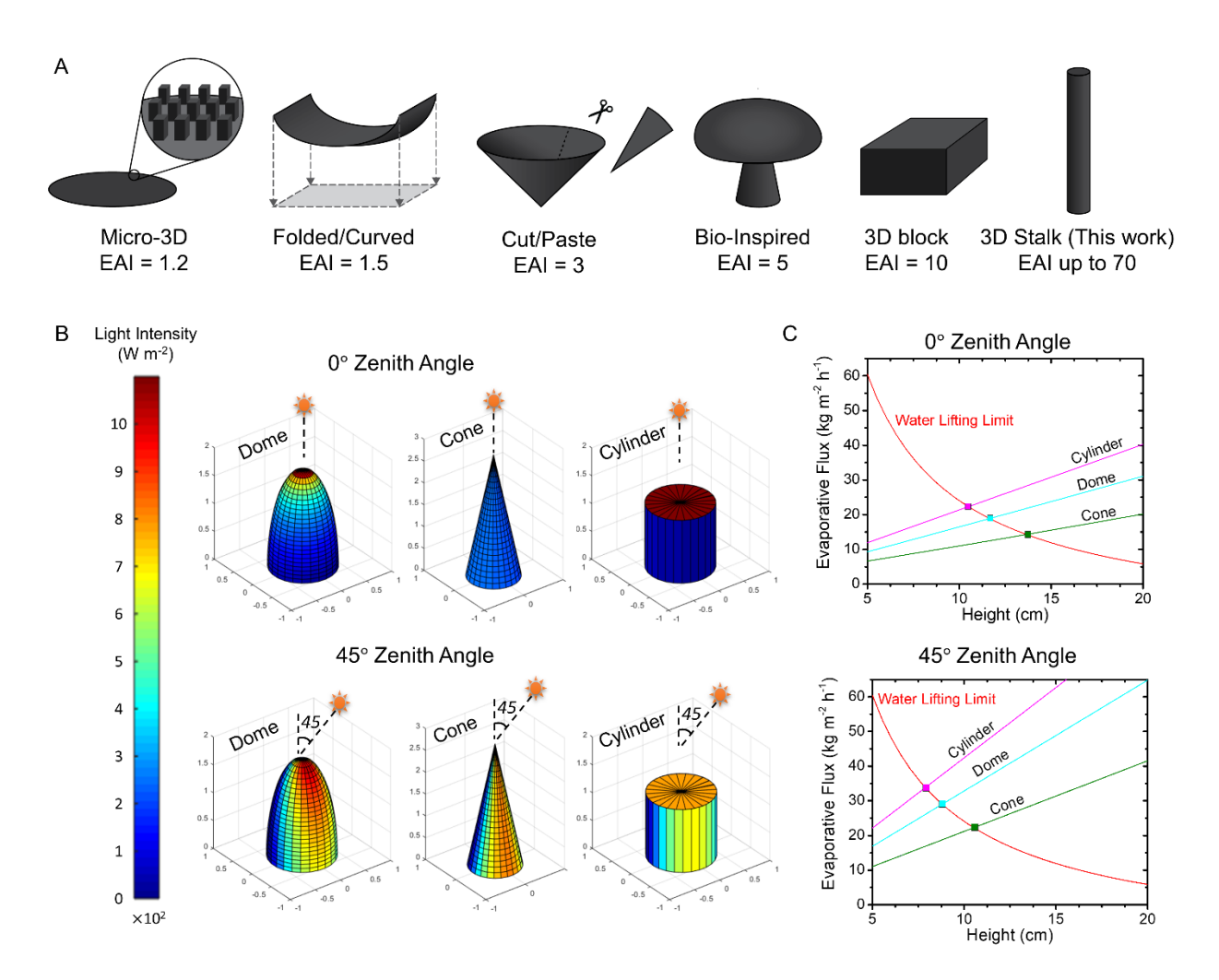


Figure 1. Comparison of different 3D evaporator geometries, and their corresponding EAI values, light absorption, and water evaporative flux. A) Comparison of 3D evaporator geometries reported in the literature ¹³⁻²⁶ and their corresponding EAI values. B) Light intensity irradiated onto three 3D geometries (cone, dome, and cylinder) with solar zenith angles of 0° (noon position) and 45° under 1-sun conditions. C) Comparison of the projected evaporative flux of the three different 3D geometries with a set projected area and increasing height. The maximum rate achievable depends on how rapidly water can be replenished to the highest evaporative interface, denoted as the "Water Lifting Limit". The evaporative flux of each 3D evaporators will depend on the incident angle of solar radiation, therefore two solar zenith angles, 0° (top) and 45° (bottom), have been studied.

MATERIALS AND METHODS

Light Intensity Analysis and Flux Prediction to Obtain Optimal Geometry. To determine the best 3D geometry to pursue, the evaporative performance of the three 3D geometries illustrated in Figure 1B were investigated as a function of height. The diameter of the projected area (base) of

all three shapes was held constant at 1 cm, while the height was varied from 5 to 20 cm. Using MATLAB, the 3D geometries were constructed by rendering the 3D surfaces into 2D subunits, each with a specific direction and inclination angle (Figure S1A and S1B). At a light incident angle (Zenith Angle) of 0° or 45°, the light intensity being irradiated onto the 3D geometry surfaces was analyzed. Using empirical data collected on the evaporative flux of the 2D material as a function of light intensity (Figure S1C), the evaporative flux of each 2D subunit was estimated. By summing up the evaporation contributions of each 2D subunit, the total evaporative flux of the 3D geometry is determined. The detailed procedure used in the light intensity and flux analysis can be found in the Supplementary Note 1 in the SI. Material Preparation. The 3D GO stalk was synthesized using a procedure adapted from our previous work.⁶ As shown in Figure 2A, a GO coating solution was prepared by mixing 17.5 mg/mL graphene oxide (GO) suspended in water, 0.035 M NaOH, 1,4-butanediol diglycidyl ether (BDGE) and triethylenetetramine (TETA) at a volume ratio of 248: 12.4: 27: 10, while keeping all chemicals on ice. The GO coating solution was sonicated with a probe sonicator (Q500 Sonicator, Qsonica, Newtown, CT) at 40% amplitude for 4 minutes. Approximately 2.0 mL of the GO coating solution was applied to a cotton humidifying filter (0.75-cm in diameter, 15-cm in height), which served as the substrate for the 3D GO stalk. The GO-coated stalk was immediately submerged in liquid nitrogen until completely frozen and then transferred to a freeze-dryer (FreeZone 1, Labconco, Kansas City, MO) and kept at a temperature of -50°C and a pressure less than 0.2 mbar for more than 12 hours. The stalk was then placed in an oven at 100°C to crosslink GO and BDGE-TETA for 24 hours. The crosslinked 3D-GO stalk was then soaked in deionized water to dissolve chemical residual for 24 hours, dried in a 60°C oven, and stored in air at room temperature. Synthesis of the 2D GO evaporator followed the same procedure, except that the

106

107

108

109

110

111

112

113

114

115

116

117

118

119

120

121

122

123

124

125

126

127

substrate used was a filter paper coupon (4.7-cm in diameter) and approximately 0.34 mL of the

130 GO coating solution was coated on each coupon.

131 Material Characterization. The surface morphology and pore size of the 3D-GO stalk were

characterized by SEM (Gemini Ultra-55, Zeiss). The light absorption spectra for the 2D- and 3D-

evaporators were characterized using UV-Vis-Nir spectrophotometer with an integrating sphere

(ASD QualitySpec Pro, Malvern Panalytical and Cary 5000, Agilent). The thermal conductivities

were measured using a Cut-Bar method described in Supplementary Note 3.

Solar Evaporation Setup. To prepare for a solar evaporation experiment, the 3D GO stalk was placed in a 250-mL beaker filled with 200 mL of feed water. The 3D stalk was secured in place by a circular extruded polystyrene (EPS) foam that fit into the top of the beaker and had a hole in its center to hold the 3D stalk. Parafilm was wrapped around the edge of the beaker and the 3D stalk to avoid leaking water vapor from the container. The bottom of the stalk was submerged in feed water to continuously supply water to the evaporation surface under capillary action. The length of the stalk above the EPS foam represents the effective height of the 3D evaporator, and it was adjusted to 1, 7.5, and 13 cm to achieve evaporation area index (EAI) values of 6.3, 41, and 70, respectively. The EAI is defined as the ratio of total surface area for evaporation relative to the projected ground area. By this definition, a 2D evaporator has an EAI of 1, whereas the EAI of a

Equation 1.

132

133

134

135

136

137

138

139

140

141

142

143

144

145

146

150

148
$$EAI_{cylinder} = \frac{A_{total}}{A_{project}} = \frac{\frac{\pi}{4}d^2 + \pi dh}{\frac{\pi}{4}d^2} = 1 + \frac{4h}{d}$$
 Equation 1

where d is the diameter and h is the effective height of the cylindrical GO stalk. If not specified,

cylindrical 3D evaporator would increase with height. This relationship can be described by

the effective evaporative height of the 3D GO stalk was kept at 7.5-cm, corresponding to an EAI

151 value of 41.

A similar setup was used for the control evaporation experiment for 2D evaporator except that the 2D GO coupon was placed flat on the EPS foam on top of a 250-mL beaker. The feed water was transported to the 2D GO coupon by a water-absorbing sheet (Nalgene Versi-Dry Surface Protectors, Thermo Fisher Scientific) placed underneath the 2D GO coupon.

Solar Evaporation Experiments. The solar evaporation performance of the 2D or 3D evaporator was evaluated using a solar simulator (91194-1000, Newport, Irvine, CA) at an intensity of 1,000 W/m^2 at the most elevated point of light absorption. The mass evaporated over time was recorded every minute using a mass balance, while the surface temperature was monitored periodically using a Ti100 infrared camera. The ambient conditions were monitored using temperature-humidity sensors (DHT22, Adafruit Industries), reporting temperatures between 25 - 35°C and relative humidity between 20 - 40%.

The evaporative flux as a function of zenith angle was measured by angling the 2D and 3D evaporators relative to the fixed light source by 20°, 40°, 60°, and 75°. For the 2D evaporator, this was achieved by using an extended water transporter and elevating the EPS base with aluminum foil. This modified base could then be angled to the specified zenith angles.

The evaporative flux as a function of wind speed was measured by placing a variable speed fan (Thermaltake, Taipei, Taiwan) about 10-cm away from the evaporator surface. Using an anemometer (Flexzion), the wind speed generated by the fan at the material surface was measured to be approximately 1.3, 1.9, and 3.5 m/s.

The evaporative flux as a function of salinity was measured by varying the NaCl concentration in the feed solution. The salt concentration tested included 3.5, 7.0, 10.5, 14.0, 17.5 wt % NaCl, representing 1x, 2x, 3x, 4x, and 5x typical seawater salt concentration (3.5 wt %). A long-term scaling test was run with 17.5 wt % NaCl, under 1-sun conditions (1 kW/m²) for 45

hours.

RESULTS AND DISCUSSION

3D-Geometric Design. To determine the optimal geometry and guide the rational design of a 3D structure for solar evaporation, we used MATLAB to predict the evaporative flux rates of different 3D structures under varying incident light angles. We first analyzed the variation of solar intensity on the 3D structure surfaces at zenith angles of 0° (solar noon position) and 45°. Analyzing the performance of 3D structures at different incident light angles is important because it illustrates how the performance of the evaporator would vary throughout the day because of solar movement. Although this daytime variability in performance is an integral feature of all evaporators, it has not been rigorously characterized until this work.

As illustrated in Figure 1B, we selected three structures (dome, cone, and cylinder) to study the effect of EAI. The light intensity on the surfaces of each of the 3D structures is not uniform due to the changing inclination angle of the surfaces. At a Zenith angle of 0°, the top surface of the 3D cylinder receives the highest light intensity, but its side surface does not receive any direct light exposure; while the light intensity on the dome and cone surfaces are weaker and distributed into a larger area. When the Zenith angle increased to 45°, all the 3D structures demonstrated larger areas being exposed to relatively high light intensity.

After translating the light intensity distribution to evaporative water flux, the total water flux for each 3D structures were calculated and plotted in Figure 1C. At both 0 and 45° Zenith angles, the cylindrical 3D structure demonstrated the highest water flux among the three geometries being studied. The advantage of the cylinder is primarily a result of the higher EAI values than that of cone or dome. For example, the EAI for the cylinder, dome, and cone at the height of 5 cm is 21, 16, and 10, respectively. The increase of structure height will result in further

increase of EAI values and corresponding increases of evaporative water flux, as illustrated in Figure 1C. However, the evaporative flux cannot increase indefinitely, as it will be eventually limited by the maximum rate at which water can be lifted to the evaporative interface by capillary forces. The maximum water lifting rate was calculated by assuming an internal pore diameter of 100 µm and a water contact angle of 0°, and the results are plotted as the water lifting limit in Figure 1C. The detailed calculation of the water lifting limit was described in the Supplementary Note 2 in SI.

198

199

200

201

202

203

204

205

206

207

208

209

210

211

212

213

214

215

216

217

218

219

220

As shown in Figure 1C, the water lifting limit decreases with increasing structure height, and its intersection with each flux line (for cylinder, cone and dome) represents the maximum achievable evaporative flux for each geometrical design. For instance, the maximum evaporative flux for a cylindrical 3D evaporator under the current design is 22 kg m⁻² h⁻¹, which was achieved at a height of 10.4 cm when the solar Zenith angle is 0°. Any increase of the cylinder height beyond 10.4 cm will not be able to further increase the evaporative flux due to the water lifting limit. At Zenith angle of 0°, the maximum evaporative flux of the cone and dome are 14 and 12 kg m⁻² h⁻¹, respectively, much lower than that of the cylinder. Similarly, when the Zenith angle is 45°, the maximum evaporative flux of the cylinder (34 kg m⁻² h⁻¹) is much higher than that of cone and dome (22 and 18 kg m⁻² h⁻¹, respectively). This analysis indicates that a cylinder represents a better 3D design than a cone or a dome as it will produce the highest EAI and evaporative water flux. Therefore, we chose the cylindrical design as the geometry of the 3D evaporator to investigate in the subsequent experiments. Note that the quantitative prediction of maximum flux or height may differ from the real experimental data as the base and pore diameters of the synthesized 3D evaporator could be different from the parameters that we assumed in the calculation. For example, the GO stalk investigated in this work has a wide range of pore sizes (Figure 2B and 2C). As a

result, higher evaporative water flux than was predicted by the model were observed due to the capillary effect induced by this pore distribution.

221

222

223

224

225

226

227

228

229

230

231

232

233

234

235

236

237

238

239

240

241

242

243

Synthesis and Characterization of Cylindrical 3D Evaporator. To synthesize a cylindrical 3D evaporator, we started with a commercially available cotton humidifying filter that serves as a substrate with high internal porosity, high hydrophilicity, and low thermal conductivity. To maximize the EAI, it is critical to have high internal porosity and hydrophilicity to increase the limits of water replenishment rate so that water lifting does not become a limiting factor for high evaporative flux. Low thermal conductivity is critical for heat localization so that the absorbed solar energy can be effectively utilized for water vaporization. To enable effective solar light absorption, the cotton stick was coated by crosslinked graphene oxide (GO) following the procedure illustrated in Figure 2A. This creates a 3D GO stalk with a light-absorbing exterior that has sub-micrometer pores (Figure 2B), while leaving the core unmodified to facilitate rapid water transport via capillary wicking (Figure 2C). Based on the SEM, the pore size between cellulosic fibers in the unmodified core ranges between 50 and 200 μm, whereas the GO coating provides much smaller pores that can be less than 0.5 µm. The heterogeneity of these pores enables the cylindrical 3D evaporator rapidly lift water through the middle of the stalk and achieve saturation, while using high capillary pressure at the evaporative interface to maintain a wet state during operation.

In addition to having an efficient water replenishment mechanism, the 3D GO stalk demonstrates high efficiencies in broadband light absorption and heat localization that greatly contribute to solar vapor generation. As shown in Figure 2D, compared to a 2D-GO control, which underwent a similar synthesis process to that of the 3D-GO stalk except that a filter paper was used as the supporting substrate,⁶ the 3D-GO stalk demonstrates higher and near-complete absorption

of light across the solar spectrum from 350 to 2500 nm. The higher absorption efficiency of the 3D-GO stalk is attributed to the thickness of the GO photo-thermal material, which allows for complete absorption of light that is transmitted by its top surface.

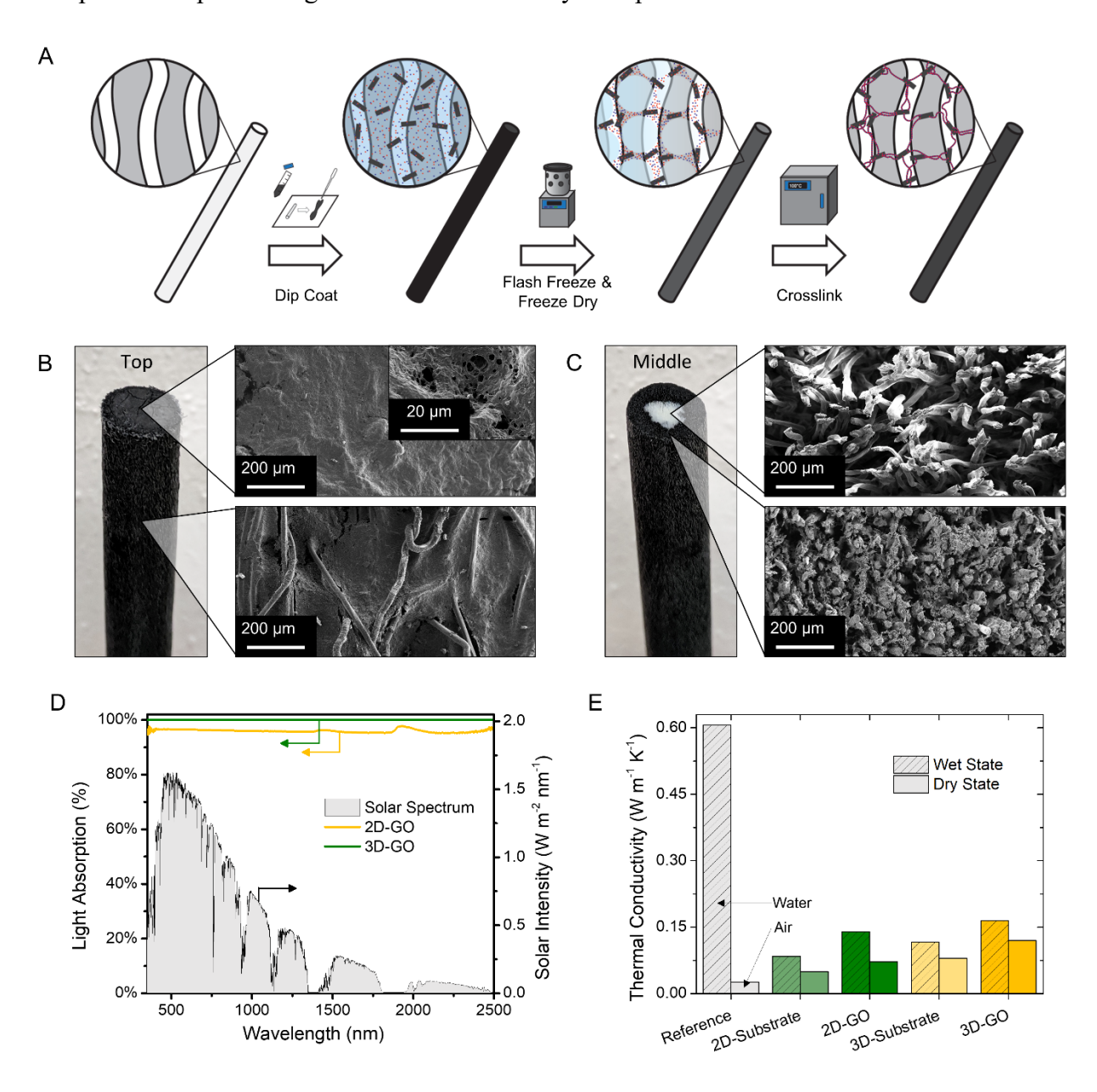


Figure 2. Synthesis and characterization of the cylindrical 3D-GO stalk. A) Synthesis of the cylindrical 3D evaporator by coating GO on a cotton stick. B) Scanning electron microcopy (SEM) images of the top (with a higher magnification insert) and side of the synthesized 3D GO stalk. C) SEM images of a cross-section from the middle of the 3D GO stalk, showing the unmodified cellulose fibers at the core and GO-modified cellulose fibers toward the outer perimeter. D) Light absorption across the solar spectrum of the 2D- and 3D-GO. E) Thermal conductivity of the 2D- and 3D- substrates and GO evaporators.

255256

257

258

259

260

261

262

263

264

265

266

267

268

269

270

271

272

273

274

275

276

277

278

In conventional 2D evaporators, heat localization at the air-water interface is achieved with a thermal insulation layer that minimizes conductive heat losses from the surface to the bulk water. To evaluate the heat localization capability, the thermal conductivity of the evaporators, as well as the unmodified substrates, was measured in both wet and dry states. Figure 2E shows that introducing the GO coating increases the thermal conductivity of both the 2D- and 3D-evaporators compared to the unmodified substrate. This is expected as the cross-linked GO replaces air in the porous substrate. As a result, the higher thermal conductivity of the crosslinked GO increases the materials' effective thermal conductivity. Similarly, the wet evaporators have higher thermal conductivities in comparison to their dry counterparts as water displaces air within the porous structure. The thermal conductivities of the wet 2D- and 3D-evaporators are 0.140 and 0.165 W m⁻¹ K⁻¹, respectively. Even though the 3D geometry results in a higher thermal conductivity, the distance over which heat must be conducted before being lost to the bulk water reservoir is significantly larger (1-13 cm) than traditional 2D evaporators (~200 µm). This dramatically reduces the overall heat loss due to conduction and maintains the heat localization that is necessary for efficient evaporation. Evaporation Performance of the 3D GO Stalk. The vapor generation performance of the 3D GO stalk was evaluated using the setup illustrated in Figure 3A. The bottom of the GO stalk was submerged in the feed water reservoir to take in water, while the stalk above the white polystyrene base provided effective area for water evaporation. By adjusting the height of the GO stalk above the base to 1, 7.5, and 13 cm, we studied the performance of the GO stalk at EAI values of 6.3, 41, 70, respectively. We also characterized the performance of a 2D GO evaporator, which by definition has an EAI value of 1. As shown in Figure 3B, operating under 1-sun conditions, increasing the EAI value beyond 1 significantly increased the evaporative flux from 1.8 (EAI =

1.0) to 34.7 (EAI = 70) kg m⁻² h⁻¹, with the corresponding dark field conditions ranging from 0.4 (EAI = 1.0) to 28.7 (EAI = 70) kg m⁻² h⁻¹.

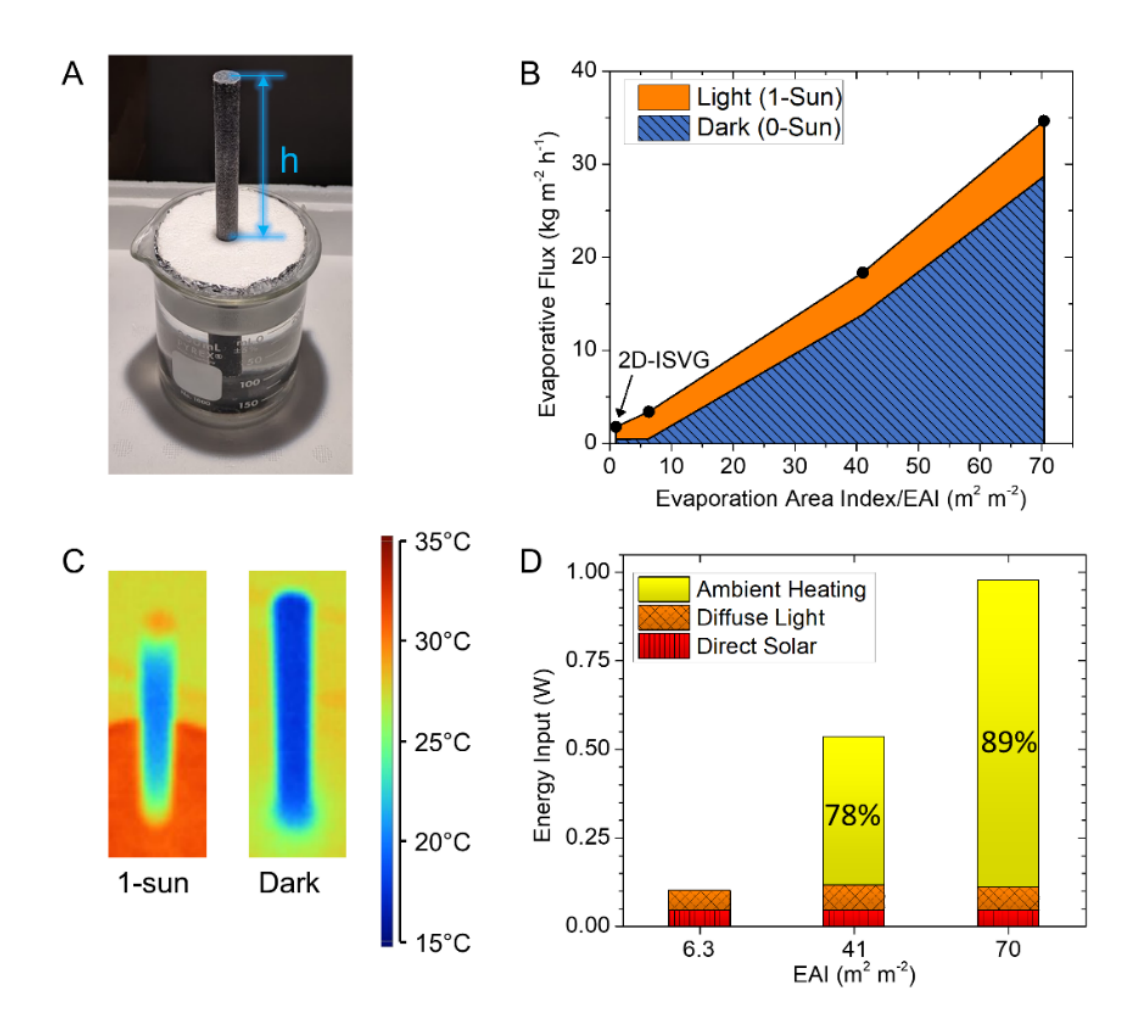


Figure 3. Evaporation performance and efficiency of the 3D evaporator. A) The experimental setup for performance characterization. B) The change of evaporative flux of the 3D GO stalk in dark and light conditions as EAI value increases. C) Thermal images of the 3D GO stalk under light and dark conditions. D) Contribution to energy input from direct solar, diffuse light, and ambient heating.

The flux enhancement can be attributed to both increased total surface area available for evaporation and more effective utilization of energy sources (e.g., ambient heating, diffuse radiation) other than the solar energy input. For example, ambient heating can serve as an additional energy source due to convective heat transfer from the relatively warmer ambient

environment to the cooled sides of the 3D GO stalk. As demonstrated by the thermal images in Figure 3C, the side surfaces of the GO stalk that are not in direct sunlight drop to a sub-ambient temperature because of evaporative cooling. Similarly, the stalk under dark conditions is much cooler than the ambient air, enabling heat transfer from ambient environment to the evaporation surface. Comparing the evaporative performance under 1-sun and dark conditions indicates that a large percentage of water flux is attributed to the evaporation taking place under dark conditions, as shown in Figure 3B. The high evaporation flux under dark conditions confirms that the 3D GO stalk with its large EAI is capable of effectively using ambient heating compared to other geometries. Although similar behavior of drawing heat from the environment during evaporation has also been observed in other studies, ^{17,26,31} the high aspect ratio of our 3D GO stalk capitalizes on this phenomenon, allowing the GO stalk to achieve evaporative flux rates 15-20 times what has been previously reported.

As shown in Figure 3B, the evaporative flux of the 3D GO stalk with high EAI values (40-70) are more than 5 times higher than the maximum evaporative fluxes reported under 1-sun conditions.⁹ This again indicates that energy sources other than direct solar are playing a very important role in contributing to the high evaporative flux (18.4 kg m⁻² h⁻¹ for the 7.5-cm stalk and 34.7 kg m⁻² h⁻¹ for the 13-cm stalk).³² In order to understand the roles of different energy sources, the total energy input (q_{input}) can be analyzed by accounting for the three primary energy sources:

$$q_{input} = q_{solar} + q_{diffuse} + q_{ambient}$$
 Equation 2

where q_{solar} , $q_{diffuse}$, and $q_{ambient}$ are energy flows coming from direct solar radiation, diffuse radiation, and ambient heating. A full description of how each of these factors were accounted for can be found in Supplementary Note 4 and 5 in the SI. Through this analysis, the contributions from each energy sources were calculated and plotted in Figure 3D and the

corresponding evaporation efficiencies were calculated. The amount of energy from direct solar and diffuse light remains constant when the EAI value changes. However, as the EAI value increases, a growing amount of energy comes from ambient heating. For example, when EAI increases from 6 to 70, the energy contribution from ambient heating increases from 0% to 89% of total energy input, while the contribution from direct solar decreases from 44% to 4.5%. This shows that the increase in evaporative flux as the height of the GO stalk increases is primarily a result of absorbing more ambient heating. It indicates that the 3D GO stalk would generate effective evaporation in warm, dark environment even without sufficient sun light exposure. When accounting for these additional energy sources, the evaporation efficiencies were 81.6%, 83.7% and 95.3% for EAI values 6.3, 41, and 70, respectively. Overall, the 3D GO stalk can derive the energy for evaporation from multiple sources, enabling a dramatic reduction in the spatial footprint of solar evaporation. **3D-Enhanced Omnidirectional Light Utilization.** One major advantage of the 3D evaporator is its omnidirectional light utilization as the sun moves across the sky throughout the day. Most solar evaporation studies use a solar source at a fixed position, often under the optimal conditions of solar noon with a zenith angle of 0°, i.e., with the incident light perpendicular to the evaporation surface. However, understanding the effect of solar movement is critical to predict the actual performance of solar evaporators throughout the day. For 2D evaporator, an increase in the zenith angle when the sun deviates from a vertical position decreases the projected cross-section that receives solar radiation, resulting in a decrease of evaporative flux (Figure 4A). However, the 3D evaporator exhibits an opposite trend, with an increase in evaporative flux as the solar angle deviates from the noon position. The reason for this is that under solar noon conditions, the only

315

316

317

318

319

320

321

322

323

324

325

326

327

328

329

330

331

332

333

334

335

336

337

surface to receive direct radiation is the top of the cylindrical 3D stalk. As the zenith angle increases,

a greater cross-section (including a portion of the sides of the cylinder) is irradiated by sunlight, resulting in a higher evaporative flux. This is a promising result for outdoor applications of 3D GO evaporator, where higher performance may be achieved in the hours leading up to and away from solar noon. To validate these findings an open-air, outdoor test was conducted to compare the performance of the 3D GO stalk and the 2D evaporator. Over the course of the 9-hour evaporation run, the 3D GO stalk maintained an average evaporative flux of 39.98 kg m⁻² h⁻¹, while the 2D evaporator had an average evaporative flux of 1.01 kg m⁻² h⁻¹. Additional information may be found in Supplementary Note 6.

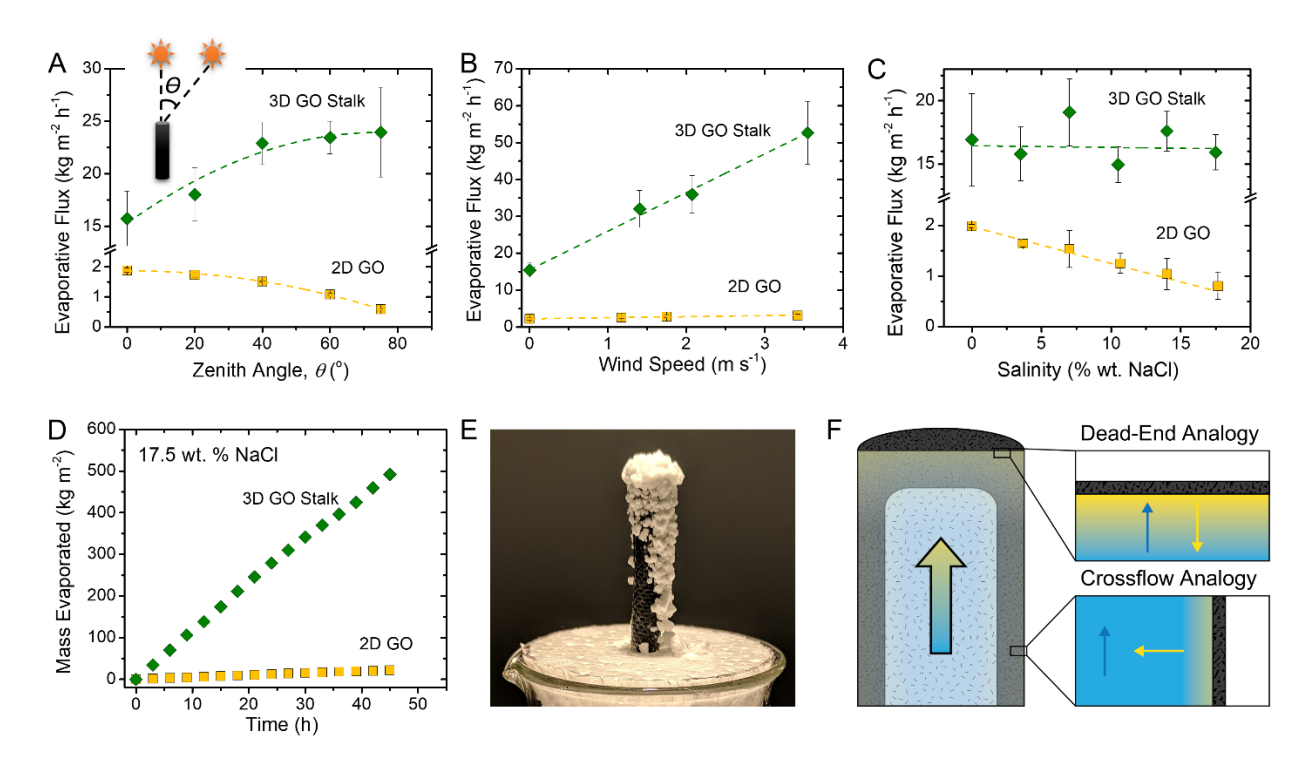


Figure 4. Enhanced evaporation performance enabled by 3D geometry. Comparison of the performance of 3D and 2D GO evaporators as a function of A) varying incident light angle, B) increasing wind speed (external forced convection rates), and C) increasing feedwater salinity. D) Mass evaporated over time with a feedwater containing 17.5 wt. % NaCl to demonstrate the constant evaporative flux observed despite scale formation. E) Scale formation on the surface of the 3D GO stalk. F) Dead-end and crossflow analogies to describe scaling behavior of the 3D-GO stalk.

3D-Enhanced Utilization of Wind Energy The second advantage of the 3D GO stalk is that it

can extract energy from the ambient environment, thus resulting in efficient utilization of convection from the wind. To demonstrate this advantage, we used a fan to artificially introduce wind at varying speeds across the 2D- and 3D-evaporators and observed significantly higher flux enhancement in the 3D evaporator than 2D. As shown in Figure 4B, when the external air flow rate increases from 0 to 3.5 m s⁻¹, the evaporative flux of the 3D GO stalk increases from 15.4 to 52.7 kg m⁻² h⁻¹, resulting in an increase of 241%; while the flux of 2D material only increases from 2.2 to 3.2 kg m⁻² h⁻¹, an increase of merely 45%. The differences between the 2D- and 3Devaporators are attributed to the geometry difference that affects the formation of the airflow boundary layer. The thickness of this boundary layer is important because water vapor molecules produced by the evaporator must diffuse through the boundary layer before convective forces sweep them away. As the rate of forced convection increases, the boundary layer thickness is compressed, decreasing the distance that water molecules must diffuse and increasing the driving force for evaporation. However, given that the average flow path length across the 2D evaporator is longer than that of the 3D evaporator, the boundary layer is still developing (and thus thinner) over a greater portion of the 3D evaporator surface area. As a result, the 3D GO stalk has a significantly higher response to increases in external convection rates than the 2D GO evaporator. This result is also promising because vapor accumulation near the evaporative interface is a severely limiting factor for vapor production in closed systems (such as a traditional solar still) that aim to condense the water vapor. Introducing external forced convection not only increases the rate of evaporation, but also could contribute to moving water vapor into a separate stage for condensation if water recovery is desired. Furthermore, in open systems (such as for evaporation ponds), the 3D GO stalk could take utilize naturally occurring wind to enhance performance.

356

357

358

359

360

361

362

363

364

365

366

367

368

369

370

371

372

373

374

375

376

377

Resilience to Mineral Scaling. A final unexpected, but exciting advantage of the 3D GO stalk is its capability of maintaining high evaporative flux when feedwater salinity increases. As shown in Figure 4C, the evaporative flux of the 3D GO stalk remains almost constant at 16.0 kg m⁻² h⁻¹ over the range of 0 to 17.5 wt. % NaCl, demonstrating a resilience to increasing feedwater salinities which resemble brines that can currently only be treated with energy intensive thermal brine concentrators. The flux of 2D GO evaporator decreases from 2 to 0.5 kg m⁻² h⁻¹ under these same conditions, which is expected due to the reduction in vapor pressure caused by increasing feedwater salinity, consistent with what we reported in an earlier study.^{6,7} In addition, the high flux of 3D GO stalk is not affected by the accumulation of salt on the evaporative surface. As seen in Figure 4D, the evaporated mass of water for both 2D- and 3D-evaporators increases at a relatively constant rate during the course of a continuous 45-h evaporation run, despite significant salt accumulation can be observed on both 2D (presented in our previous publication⁶) and 3D material surfaces (Figure 4E) at such high salt concentration (17.5 wt. % NaCl) in feedwater. Note that further studies are needed to investigate the effects of more complicated mineral composition on this behavior.³³ Nevertheless, with pure NaCl the continuous high flux of the 3D stalk results in the vaporization of a total of 492 kg of water per m² throughout the 45-h period, while under the same condition the 2D GO evaporator would only vaporize 22 kg of water per m². Such a high evaporation rate for a salinity that is 5 times more concentrated than seawater demonstrates the potential of the 3D GO stalk for brine concentration and ZLD applications.

379

380

381

382

383

384

385

386

387

388

389

390

391

392

393

394

395

396

397

398

399

400

401

To explain why the 3D GO stalk has better resistance to these high salinities compared to its 2D counterpart, we illustrate the transport process in the 3D stalk using an analogy from membrane filtration (Figure 4F). The evaporation process on the top surface of the stalk is analogous to a dead-end filtration, which results in extreme concentration polarization because the

direction of water flow opposes the direction of the back-diffusion of salt, creating a higher salt concentration at the evaporative interface on top of the 3D GO stalk. These high salt concentrations lower the saturation vapor pressure at the evaporative interface, thus lowering the driving force for evaporation and decreasing the flux. Since the evaporation on the entire 2D evaporator is like deadend filtration, its performance is prone to the negative impacts of high salt concentration. However, such an effect on the performance of the 3D GO stalk is greatly diminished because the top surface evaporation constitutes a small portion of the total evaporative surface area (only 2.4% for this experiment). Meanwhile, the side surfaces of the 3D GO stalk benefit from crossflow, where the back-diffusion of salt ions is accelerated by the upward flow of water through the 3D stalk. Therefore, the reduced concentration polarization on the sides may slow down the accumulation of salts and contribute to maintaining a constant evaporative flux for the 3D GO stalk. While the precipitation of salt on the surface of the 3D GO stalk (Figure 4E) increases the albedo of the 3D GO stalk and decreases the light available for evaporation, the negative impact of this on evaporative flux is mitigate by the fact that a significant portion of energy from evaporation is coming from sources other than direct light irradiation (i.e., diffuse light and ambient heating).

Furthermore, the precipitation of salt onto the surface of the 3D GO stalk (Figure 4E) presents another promising opportunity in ZLD, *i.e.*, mineral recovery. As salt crystals grow on the sides of the cylindrical 3D evaporator, they gradually become unstable and naturally slough off the cylindrical structure. This process could be engineered into a passive salt management strategy that simultaneously prevents excessive buildup of salt on the 3D structure while collecting crystallized salt with valorization application.

423

424

422

402

403

404

405

406

407

408

409

410

411

412

413

414

415

416

417

418

419

420

421

Technology Outlook for the 3D GO Stalk. This study explored a variety of advantages of using

3D GO stalk for brine treatment in comparison with 2D evaporators. As summarized in Figure 5A, our cylindrical design significantly increases the EAI value, enabling high evaporative flux that is about 100 times faster than a traditional evaporation pond. The flux enhancement is also attributed to more efficient use of ambient heating and omnidirectional light utilization. In addition, the 3D GO stalk is capable of maintaining high flux in highly concentrated brine and demonstrates potential for mineral recovery. We also compared the performance of the 3D GO stalk with published literature on other 3D structures. As shown in Figure 5B, this study is one of two studies with EAI values greater than 30 (see Supplementary Note 7 for full details). Most structures have low evaporative fluxes (less than 5 kg m⁻² h⁻¹) due to relatively low EAI values. Most structures have some other studies demonstrate 3D evaporators with moderate EAI values, they do not achieve comparable evaporative flux rates owing to self-inhibiting structures, *i.e.*, their geometries prevent the diffusion of water vapor away from the evaporator, creating high-humidity pockets near the evaporative interface that diminish the driving force for evaporation. 24,25,36-38

The high evaporative flux combined with the passive salt management strategy demonstrated in this work indicated that the 3D GO stalk has the potential to significantly reduce the spatial and energy footprint of brine treatment. If paired with upstream purification steps, the 3D GO stalk could be used for continuous production of mineral resources for salt mining or resource recovery operations. Further investigation is still needed to study the effects of scaling up to a treatment system that contains large number of GO stalks and to evaluate the fouling performance under long-term operation with realistic feed streams. Nevertheless, the 3D GO stalk has demonstrated the ability to significantly reduce the spatial footprint of the solar evaporation process while passively processing brines with salt concentration as high as 17.5 wt%, bringing the field one step closer toward the development of a sustainable off-grid desalination technology

with ZLD and salt recovery.

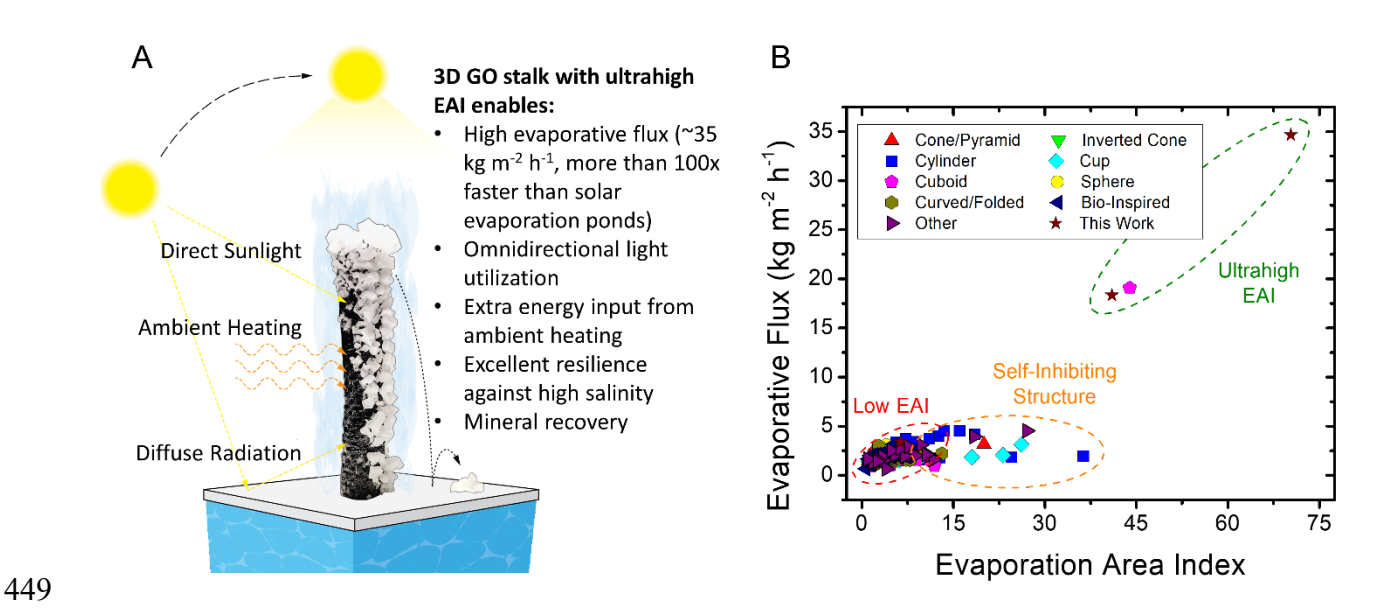


Figure 5. Comparison of the performance of the GO stalk to other 3D evaporators. A) Summary of the advantages of 3D GO stalk. B) Comparison of our work with the evaporative flux of 3D evaporators reported through June 2021. 11,15–31,34–72 The data were all obtained under 1-sun conditions.

Associated Content

Supporting Information

The Supporting Information is available free of charge on the ACS Publications website. This document includes additional analysis of different 3D geometries, determination of water lifting limit, analysis of convective heat transfer for ambient heating, analysis of solar energy input from direct solar and diffuse light, compilation of 3D evaporator performance data, and thermal conductivity measurements by Cut-Bar Method.

Acknowledgements

- The material is based upon work supported by the U.S. National Science Foundation under award
- no. CBET-1706059, Graduate Research Fellowship under award no. DGE-1106400, the InFEWS
- 466 Fellowship under award no. 1633740, and Rudd Family Foundation's Big Ideas Competition.
- Work at the Molecular Foundry was supported by the Office of Science, Office of Basic Energy
- Sciences, of the U.S. Department of Energy under award no. DE-AC02-05CH11231. A.M.
- acknowledges funding support from the ITRI-Rosenfeld Fellowship from the Energy Technologies
- 470 Area at Lawrence Berkeley National Laboratory. This research was also supported by the National
- 471 Science Foundation Engineering Research Center for Reinventing the Nation's Urban Water
- 472 Infrastructure (ReNUWIt EEC-1028968). However, the opinions expressed herein are those of the
- authors and do not necessarily reflect those of the sponsors.

References

- 475 (1) Leflaive, X. Water Outlook to 2050: The OECD Calls for Early and Strategic Action. *GWF* 476 *Discuss. Pap. 1219, Glob. Water Forum, Canberra, Aust.* **2012**, 1–9.
- 477 (2) Kundzewicz, Z. W.; Krysanova, V. Climate Change and Stream Water Quality in the Multi-478 Factor Context. *Clim. Change* **2010**, *103* (3), 353–362. https://doi.org/10.1007/s10584-010-479 9822-9.
- 480 (3) Schlosser, C. A.; Strzepek, K.; Gao, X.; Fant, C.; Blanc, É.; Paltsev, S.; Jacoby, H.; Reilly, J.; Gueneau, A. The Future of Global Water Stress: An Integrated Assessment. *Earth's Futur.* 2014, 2 (8), 341–361. https://doi.org/10.1002/2014ef000238.
- 483 (4) Sarai Atab, M.; Smallbone, A. J.; Roskilly, A. P. An Operational and Economic Study of a Reverse Osmosis Desalination System for Potable Water and Land Irrigation. *Desalination* **2016**, *397*, 174–184. https://doi.org/10.1016/j.desal.2016.06.020.
- 486 (5) Xu, P.; Cath, T. Y.; Robertson, A. P.; Reinhard, M.; Leckie, J. O.; Drewes, J. E. Critical 487 Review of Desalination Concentrate Management, Treatment and Beneficial Use. *Environ*. 488 *Eng. Sci.* **2013**, *30* (8), 502–514. https://doi.org/10.1089/ees.2012.0348.
- 489 (6) Finnerty, C.; Zhang, L.; Sedlak, D. L.; Nelson, K. L.; Mi, B. Synthetic Graphene Oxide Leaf 490 for Solar Desalination with Zero Liquid Discharge. *Environ. Sci. Technol.* **2017**, *51* (20), 491 11701–11709. https://doi.org/10.1021/acs.est.7b03040.
- 492 (7) Menon, A. K.; Haechler, I.; Kaur, S.; Lubner, S.; Prasher, R. S. Enhanced Solar Evaporation 493 Using a Photo-Thermal Umbrella for Wastewater Management. *Nat. Sustain.* **2020**, *3* (2), 494 144–151. https://doi.org/10.1038/s41893-019-0445-5.
- 495 (8) Ghasemi, H.; Ni, G.; Marconnet, A. M.; Loomis, J.; Yerci, S.; Miljkovic, N.; Chen, G. Solar 496 Steam Generation by Heat Localization. *Nat. Commun.* **2014**, *5* (1), 1–7. 497 https://doi.org/10.1038/ncomms5449.
- 498 (9) Zhao, F.; Zhou, X.; Shi, Y.; Qian, X.; Alexander, M.; Zhao, X.; Mendez, S.; Yang, R.; Qu, 499 L.; Yu, G. Highly Efficient Solar Vapour Generation via Hierarchically Nanostructured Gels. 500 Nat. Nanotechnol. **2018**, 13 (6), 489–495. https://doi.org/10.1038/s41565-018-0097-z.
- 501 (10) Liang, H.; Liao, Q.; Chen, N.; Liang, Y.; Lv, G.; Zhang, P.; Lu, B.; Qu, L. Thermal Efficiency of Solar Steam Generation Approaching 100 % through Capillary Water Transport. *Angew. Chemie* **2019**, *131* (52), 19217–19222. https://doi.org/10.1002/ange.201911457.
- 505 (11) Tang, J.; Zheng, T.; Song, Z.; Shao, Y.; Li, N.; Jia, K.; Tian, Y.; Song, Q.; Liu, H.; Xue, G. Realization of Low Latent Heat of a Solar Evaporator via Regulating the Water State in Wood Channels. *ACS Appl. Mater. Interfaces* **2020**, *12* (16), 18504–18511.

- 508 https://doi.org/10.1021/acsami.0c01261.
- Zang, L.; Sun, L.; Zhang, S.; Finnerty, C.; Kim, A.; Ma, J.; Mi, B. Nanofibrous Hydrogel-Reduced Graphene Oxide Membranes for Effective Solar-Driven Interfacial Evaporation and Desalination. *Chem. Eng. J.* 2021, 422, 129998.
 https://doi.org/10.1016/j.cej.2021.129998.
- Zhou, J.; Gu, Y.; Liu, P.; Wang, P.; Miao, L.; Liu, J.; Wei, A.; Mu, X.; Li, J.; Zhu, J. Development and Evolution of the System Structure for Highly Efficient Solar Steam Generation from Zero to Three Dimensions. *Advanced Functional Materials*. December 13, 2019, p 1903255. https://doi.org/10.1002/adfm.201903255.
- 517 (14) Mi, B.; Finnerty, C.; Conway, K. Prospects of Artificial Tree for Solar Desalination. *Current Opinion in Chemical Engineering*. Elsevier Ltd September 1, 2019, pp 18–25. https://doi.org/10.1016/j.coche.2019.06.004.
- 520 (15) Zhang, P.; Liao, Q.; Yao, H.; Cheng, H.; Huang, Y.; Yang, C.; Jiang, L.; Qu, L. Three-521 Dimensional Water Evaporation on a Macroporous Vertically Aligned Graphene Pillar 522 Array under One Sun. *J. Mater. Chem. A* **2018**, *6* (31), 15303–15309. 523 https://doi.org/10.1039/c8ta05412f.
- 524 (16) Yu, Z.; Cheng, S.; Li, C.; Li, L.; Yang, J. Highly Efficient Solar Vapor Generator Enabled 525 by a 3D Hierarchical Structure Constructed with Hydrophilic Carbon Felt for Desalination 526 and Wastewater Treatment. *ACS Appl. Mater. Interfaces* **2019**, *11* (35), 32038–32045. 527 https://doi.org/10.1021/acsami.9b08480.
- 528 (17) Song, H.; Liu, Y.; Liu, Z.; Singer, M. H.; Li, C.; Cheney, A. R.; Ji, D.; Zhou, L.; Zhang, N.; 529 Zeng, X.; Bei, Z.; Yu, Z.; Jiang, S.; Gan, Q. Cold Vapor Generation beyond the Input Solar Energy Limit. *Adv. Sci.* **2018**, *5* (8), 1800222. https://doi.org/10.1002/advs.201800222.
- 531 (18) Hong, S.; Shi, Y.; Li, R.; Zhang, C.; Jin, Y.; Wang, P. Nature-Inspired, 3D Origami Solar Steam Generator toward Near Full Utilization of Solar Energy. *ACS Appl. Mater. Interfaces* **2018**, *10* (34), 28517–28524. https://doi.org/10.1021/acsami.8b07150.
- Liu, Z.; Wu, B.; Zhu, B.; Chen, Z.; Zhu, M.; Liu, X. Continuously Producing Watersteam
 and Concentrated Brine from Seawater by Hanging Photothermal Fabrics under Sunlight.
 Adv. Funct. Mater. 2019, 29 (43), 1905485. https://doi.org/10.1002/adfm.201905485.
- 537 (20) Li, X.; Lin, R.; Ni, G.; Xu, N.; Hu, X.; Zhu, B.; Lv, G.; Li, J.; Zhu, S.; Zhu, J. Three-538 Dimensional Artificial Transpiration for Efficient Solar Waste-Water Treatment. *Natl. Sci.* 539 *Rev.* **2017**, *5* (1), 70–77. https://doi.org/10.1093/nsr/nwx051.
- Wang, Y.; Wang, C.; Song, X.; Huang, M.; Megarajan, S. K.; Shaukat, S. F.; Jiang, H. Improved Light-Harvesting and Thermal Management for Efficient Solar-Driven Water Evaporation Using 3D Photothermal Cones. *J. Mater. Chem. A* **2018**, *6* (21), 9874–9881. https://doi.org/10.1039/c8ta01469h.
- 544 (22) Ni, F.; Xiao, P.; Zhang, C.; Liang, Y.; Gu, J.; Zhang, L.; Chen, T. Micro-/Macroscopically 545 Synergetic Control of Switchable 2D/3D Photothermal Water Purification Enabled by 546 Robust, Portable, and Cost-Effective Cellulose Papers. *ACS Appl. Mater. Interfaces* **2019**, 547 *I1* (17), 15498–15506. https://doi.org/10.1021/acsami.9b00380.
- 548 (23) Xu, N.; Hu, X.; Xu, W.; Li, X.; Zhou, L.; Zhu, S.; Zhu, J. Mushrooms as Efficient Solar 549 Steam-Generation Devices. *Adv. Mater.* **2017**, *29* (28), 1606762. 550 https://doi.org/10.1002/adma.201606762.
- 551 (24) Bian, Y.; Shen, Y.; Tang, K.; Du, Q.; Hao, L.; Liu, D.; Hao, J.; Zhou, D.; Wang, X.; Zhang, 552 H.; Li, P.; Sang, Y.; Yuan, X.; Zhao, L.; Ye, J.; Liu, B.; Lu, H.; Yang, Y.; Zhang, R.; Zheng, Y.; Xiong, X.; Gu, S. Carbonized Tree-Like Furry Magnolia Fruit-Based Evaporator

- Replicating the Feat of Plant Transpiration. *Glob. Challenges* **2019**, *3* (10), 1900040. https://doi.org/10.1002/gch2.201900040.
- Xiao, P.; He, J.; Liang, Y.; Zhang, C.; Gu, J.; Zhang, J.; Huang, Y.; Kuo, S.-W.; Chen, T. Rationally Programmable Paper-Based Artificial Trees Toward Multipath Solar-Driven Water Extraction from Liquid/Solid Substrates. *Sol. RRL* **2019**, *3* (7), 1900004. https://doi.org/10.1002/solr.201900004.
- 560 (26) Shi, Y.; Li, R.; Jin, Y.; Zhuo, S.; Shi, L.; Chang, J.; Hong, S.; Ng, K. C.; Wang, P. A 3D Photothermal Structure toward Improved Energy Efficiency in Solar Steam Generation.

 562 Joule 2018, 2 (6), 1171–1186. https://doi.org/10.1016/j.joule.2018.03.013.
- Yang, Q.; Xu, C.; Wang, F.; Ling, Z.; Zhang, Z.; Fang, X. A High-Efficiency and Low-Cost Interfacial Evaporation System Based on Graphene-Loaded Pyramid Polyurethane Sponge for Wastewater and Seawater Treatments. *ACS Appl. Energy Mater.* **2019**, *2* (10), 7223–7232. https://doi.org/10.1021/acsaem.9b01201.
- 567 (28) Lu, Y.; Fan, D.; Xu, H.; Min, H.; Lu, C.; Lin, Z.; Yang, X. Implementing Hybrid Energy 568 Harvesting in 3D Spherical Evaporator for Solar Steam Generation and Synergic Water 569 Purification. *Sol. RRL* **2020**, *4* (9), 2000232. https://doi.org/10.1002/solr.202000232.
- 570 (29) Tu, C.; Cai, W.; Chen, X.; Ouyang, X.; Zhang, H.; Zhang, Z. A 3D-Structured Sustainable 571 Solar-Driven Steam Generator Using Super-Black Nylon Flocking Materials. *Small* **2019**, 572 *15* (37), 1902070. https://doi.org/10.1002/smll.201902070.
- 573 (30) Li, J.; Wang, X.; Lin, Z.; Xu, N.; Li, X.; Liang, J.; Zhao, W.; Lin, R.; Zhu, B.; Liu, G.; Zhou, 574 L.; Zhu, S.; Zhu, J. Over 10 Kg M-2 H-1 Evaporation Rate Enabled by a 3D Interconnected 575 Porous Carbon Foam. *Joule* **2020**, *0* (0). https://doi.org/10.1016/j.joule.2020.02.014.
- 576 (31) Li, X.; Li, J.; Lu, J.; Xu, N.; Chen, C.; Min, X.; Zhu, B.; Li, H.; Zhou, L.; Zhu, S.; Zhang,
 577 T.; Zhu, J. Enhancement of Interfacial Solar Vapor Generation by Environmental Energy.
 578 Joule 2018, 2 (7), 1331–1338. https://doi.org/10.1016/j.joule.2018.04.004.
- 579 (32) Li, X.; Ni, G.; Cooper, T.; Xu, N.; Li, J.; Zhou, L.; Hu, X.; Zhu, B.; Yao, P.; Zhu, J. Measuring Conversion Efficiency of Solar Vapor Generation. *Joule*. Cell Press August 21, 2019, pp 1798–1803. https://doi.org/10.1016/j.joule.2019.06.009.
- 582 Zang, L.; Finnerty, C.; Zheng, S.; Conway, K.; Sun, L.; Ma, J.; Mi, B. Interfacial Solar Vapor 583 Generation for Desalination and Brine Treatment: Evaluating Current Strategies of Solving 584 Scaling. Water Research. Elsevier Ltd 15. 117135. June 2021, 585 https://doi.org/10.1016/j.watres.2021.117135.
- 586 (34) Xu, Y.; Ma, J.; Liu, D.; Xu, H.; Cui, F.; Wang, W. Origami System for Efficient Solar Driven 587 Distillation in Emergency Water Supply. *Chem. Eng. J.* **2019**, *356* (September 2018), 869– 588 876. https://doi.org/10.1016/j.cej.2018.09.070.
- 589 (35) Li, W.; Li, Z.; Bertelsmann, K.; Fan, D. E. Portable Low-Pressure Solar Steaming-590 Collection Unisystem with Polypyrrole Origamis. *Adv. Mater.* **2019**, *31* (29), 1900720. 591 https://doi.org/10.1002/adma.201900720.
- 592 (36) Sun, P.; Zhang, W.; Zada, I.; Zhang, Y.; Gu, J.; Liu, Q.; Su, H.; Pantelić, D.; Jelenković, B.; Zhang, D. 3D-Structured Carbonized Sunflower Heads for Improved Energy Efficiency in Solar Steam Generation. *ACS Appl. Mater. Interfaces* **2020**, *12* (2), 2171–2179. https://doi.org/10.1021/acsami.9b11738.
- 596 (37) Sui, Y.; Hao, D.; Guo, Y.; Cai, Z.; Xu, B. A Flowerlike Sponge Coated with Carbon Black 597 Nanoparticles for Enhanced Solar Vapor Generation. *J. Mater. Sci.* **2020**, *55* (1), 298–308. 598 https://doi.org/10.1007/s10853-019-03977-9.
- 599 (38) Gao, X.; Lan, H.; Li, S.; Lu, X.; Zeng, M.; Gao, X.; Wang, Q.; Zhou, G.; Liu, J.-M.;

- Naughton, M. J.; Kempa, K.; Gao, J. Artificial Mushroom Sponge Structure for Highly Efficient and Inexpensive Cold-Water Steam Generation. *Glob. Challenges* **2018**, *2* (12), 1800035. https://doi.org/10.1002/gch2.201800035.
- 603 (39) Chen, Y.; Zhao, G.; Ren, L.; Yang, H.; Xiao, X.; Xu, W. Blackbody-Inspired Array Structural Polypyrrole-Sunflower Disc with Extremely High Light Absorption for Efficient Photothermal Evaporation. *ACS Appl. Mater. Interfaces* **2020**, *12* (41), 46653–46660. https://doi.org/10.1021/acsami.0c11549.
- 607 (40) Wang, H.; Zhang, C.; Zhang, Z.; Zhou, B.; Shen, J.; Du, A. Artificial Trees Inspired by
 608 Monstera for Highly Efficient Solar Steam Generation in Both Normal and Weak Light
 609 Environments. Adv. Funct. Mater. 2020, 30 (48), 2005513.
 610 https://doi.org/10.1002/adfm.202005513.
- 611 Liu, J.; Yao, J.; Yuan, Y.; Liu, Q.; Zhang, W.; Zhang, X.; Gu, J. Surface-Carbonized (41)612 Bamboos with Multilevel Functional Biostructures Deliver High Photothermal Water 613 Evaporation Performance. Adv. Sustain. Syst. 2020, 4 (9),2000126. 614 https://doi.org/10.1002/adsu.202000126.
- 615 (42) Chen, S.; Sun, Z.; Xiang, W.; Shen, C.; Wang, Z.; Jia, X.; Sun, J.; Liu, C.-J. Plasmonic 616 Wooden Flower for Highly Efficient Solar Vapor Generation. *Nano Energy* **2020**, 104998. 617 https://doi.org/10.1016/j.nanoen.2020.104998.
- Kang, Q.; Hu, R.; Chen, Y.; Xiao, X.; Zhao, G.; Yang, H.; Li, J.; Xu, W.; Wang, X. Banyan Inspired Hierarchical Evaporators for Efficient Solar Photothermal Conversion. *Appl. Energy* 2020, 276, 115545. https://doi.org/10.1016/j.apenergy.2020.115545.
- 621 (44) Geng, Y.; Sun, W.; Ying, P.; Zheng, Y.; Ding, J.; Sun, K.; Li, L.; Li, M. Bioinspired Fractal
 622 Design of Waste Biomass-Derived Solar—Thermal Materials for Highly Efficient Solar
 623 Evaporation. *Adv. Funct. Mater.* **2020**, *31* (3), 2007648.
 624 https://doi.org/10.1002/adfm.202007648.
- (45) Xie, Z.; Zhu, J.; Zhang, L. Three-Dimensionally Structured Polypyrrole-Coated Setaria
 Viridis Spike Composites for Efficient Solar Steam Generation. ACS Appl. Mater. Interfaces
 2021, 13 (7), 9027–9035. https://doi.org/10.1021/acsami.0c22917.
- 628 (46) Sun, Y.; Zhao, Z.; Zhao, G.; Wang, L.; Jia, D.; Yang, Y.; Liu, X.; Wang, X.; Qiu, J. High 629 Performance Carbonized Corncob-Based 3D Solar Vapor Steam Generator Enhanced by 630 Environmental Energy. *Carbon N. Y.* **2021**, *179*, 337–347. 631 https://doi.org/10.1016/j.carbon.2021.04.037.
- Kang, C.; Yuan, B.; Liang, Y.; Yang, L.; Bai, L.; Yang, H.; Wei, D.; Wang, W.; Chen, H.
 Solar Vapor Generator: A Natural All-in-One 3D System Derived from Cattail. Sol. Energy
 Mater. Sol. Cells 2021, 227, 111127. https://doi.org/10.1016/j.solmat.2021.111127.
- 635 (48) Yang, Y.; Sui, Y.; Cai, Z.; Xu, B. Low-Cost and High-Efficiency Solar-Driven Vapor Generation Using a 3D Dyed Cotton Towel. *Glob. Challenges* **2019**, *3* (9), 1900004. https://doi.org/10.1002/gch2.201900004.
- 638 (49)Wu, L.; Dong, Z.; Cai, Z.; Ganapathy, T.; Fang, N. X.; Li, C.; Yu, C.; Zhang, Y.; Song, Y. 639 Highly Efficient Three-Dimensional Solar Evaporator for High Salinity Desalination by 640 Localized Crystallization. 2020, Nat. Commun. 11 (1),1-12.641 https://doi.org/10.1038/s41467-020-14366-1.
- Kang, Y.; Ravi, S. K.; Tan, S. C. Systematic Study of the Effects of System Geometry and Ambient Conditions on Solar Steam Generation for Evaporation Optimization. *Adv. Sustain. Syst.* 2019, *3* (8), 1900044. https://doi.org/10.1002/adsu.201900044.
- 645 (51) Guo, C.; Zhao, J.; Zhang, W.; Miao, E.; Xie, Y. Constructing 3D Optical Absorption Holes

- by Stacking Macroporous Membrane for Highly Efficient Solar Steam Generation. *Renew. Energy* **2020**, *159*, 944–953. https://doi.org/10.1016/j.renene.2020.06.051.
- Shao, B.; Wu, X.; Wang, Y.; Gao, T.; Liu, Z. Q.; Owens, G.; Xu, H. A General Method for Selectively Coating Photothermal Materials on 3D Porous Substrate Surfaces towards Cost-Effective and Highly Efficient Solar Steam Generation. J. Mater. Chem. A 2020, 8 (46), 24703–24709. https://doi.org/10.1039/d0ta08539a.
- 652 Zhang, X.; Yang, L.; Dang, B.; Tao, J.; Li, S.; Zhao, S.; Li, W.; Li, J.; Chen, Z.; Liu, S. 653 Nature-Inspired Design: P- Toluenesulfonic Acid-Assisted Hydrothermally Engineered 654 Generation. for Solar Steam Nano Energy 105322. 2020, *78*. 655 https://doi.org/10.1016/j.nanoen.2020.105322.
- 656 (54) Bian, Y.; Du, Q.; Tang, K.; Shen, Y.; Hao, L.; Zhou, D.; Wang, X.; Xu, Z.; Zhang, H.; Zhao,
 657 L.; Zhu, S.; Ye, J.; Lu, H.; Yang, Y.; Zhang, R.; Zheng, Y.; Gu, S. Carbonized Bamboos as
 658 Excellent 3D Solar Vapor-Generation Devices. *Adv. Mater. Technol.* 2019, 4 (4), 1800593.
 659 https://doi.org/10.1002/admt.201800593.
- Li, Z.; Wang, C.; Lei, T.; Ma, H.; Su, J.; Ling, S.; Wang, W. Arched Bamboo Charcoal as
 Interfacial Solar Steam Generation Integrative Device with Enhanced Water Purification
 Capacity. Adv. Sustain. Syst. 2019, 3 (4), 1800144. https://doi.org/10.1002/adsu.201800144.
- (56) Wu, X.; Wu, L.; Tan, J.; Chen, G. Y.; Owens, G.; Xu, H. Evaporation above a Bulk Water
 Surface Using an Oil Lamp Inspired Highly Efficient Solar-Steam Generation Strategy. J.
 Mater. Chem. A 2018, 6 (26), 12267–12274. https://doi.org/10.1039/c8ta03280g.
- (57) Wu, X.; Gao, T.; Han, C.; Xu, J.; Owens, G.; Xu, H. A Photothermal Reservoir for Highly
 Efficient Solar Steam Generation without Bulk Water. *Sci. Bull.* 2019, 64 (21), 1625–1633.
 https://doi.org/10.1016/j.scib.2019.08.022.
- (58) Storer, D. P.; Phelps, J. L.; Wu, X.; Owens, G.; Khan, N. I.; Xu, H. Graphene and Rice Straw-Fiber-Based 3D Photothermal Aerogels for Highly Efficient Solar Evaporation. ACS
 Appl. Mater. Interfaces 2020, acsami.0c01707. https://doi.org/10.1021/acsami.0c01707.
- 672 (59) Wang, L.; Liu, C.; Wang, H.; Xu, Y.; Ma, S.; Zhuang, Y.; Xu, W.; Cui, W.; Yang, H. Three-673 Dimensional Wood-Inspired Bilayer Membrane Device Containing Microchannels for 674 Highly Efficient Solar Steam Generation. *ACS Appl. Mater. Interfaces* **2020**, *12* (21), 675 24328–24338. https://doi.org/10.1021/acsami.0c04740.
- 676 (60) Wang, Y.; Sun, X.; Tao, S. Rational 3D Coiled Morphology for Efficient Solar-Driven Desalination. *Environ. Sci. Technol.* **2020**, *54* (24), 16240–16248. https://doi.org/10.1021/acs.est.0c05449.
- 679 (61) Li, N.; Qiao, L.; He, J.; Wang, S.; Yu, L.; Murto, P.; Li, X.; Xu, X. Solar-Driven Interfacial Evaporation and Self-Powered Water Wave Detection Based on an All-Cellulose Monolithic Design. *Adv. Funct. Mater.* **2020**, 2008681. https://doi.org/10.1002/adfm.202008681.
- 682 (62) Gao, T.; Wu, X.; Owens, G.; Xu, H.-L. A Cobalt Oxide@polydopamine-Reduced Graphene
 683 Oxide-Based 3D Photothermal Evaporator for Highly Efficient Solar Steam Generation.
 684 Tungsten 2020, 1–10. https://doi.org/10.1007/s42864-020-00062-6.
- 685 (63) Gao, T.; Wu, X.; Wang, Y.; Owens, G.; Xu, H. A Hollow and Compressible 3D Photothermal Evaporator for Highly Efficient Solar Steam Generation without Energy Loss. *Sol. RRL* **2021**, *5* (5), 2100053. https://doi.org/10.1002/solr.202100053.
- 688 (64) Bai, B.; Yang, X.; Tian, R.; Ren, W.; Suo, R.; Wang, H. High-Efficiency Solar Steam 689 Generation Based on Blue Brick-Graphene Inverted Cone Evaporator. *Appl. Therm. Eng.* 690 **2019**, *163*, 114379. https://doi.org/10.1016/j.applthermaleng.2019.114379.
- 691 (65) Cao, N.; Lu, S.; Yao, R.; Liu, C.; Xiong, Q.; Qin, W.; Wu, X. A Self-Regenerating Air-Laid

- Paper Wrapped ASA 3D Cone-Shaped Janus Evaporator for Efficient and Stable Solar Desalination. *Chem. Eng. J.* **2020**, *397*, 125522. https://doi.org/10.1016/j.cej.2020.125522.
- 694 (66) Xu, Y.; Xu, T.; Wang, J. J.; Liu, W.; Wang, J. J. Microvessel-Assisted Environmental 695 Thermal Energy Extraction Enabling 24-Hour Continuous Interfacial Vapor Generation. 696 ChemSusChem 2020, No. 13, 1–9. https://doi.org/10.1002/cssc.202002238.
- 697 (67) Yuan, B.; Zhang, C.; Liang, Y.; Yang, L.; Yang, H.; Bai, L.; Wei, D.; Wang, W.; Wang, Q.; Chen, H. A Low-Cost 3D Spherical Evaporator with Unique Surface Topology and Inner Structure for Solar Water Evaporation-Assisted Dye Wastewater Treatment. *Adv. Sustain.* 5yst. 2020, 2000245. https://doi.org/10.1002/adsu.202000245.
- Wang, Y.; Liang, W.; Liang, F.; Wang, C.; Song, X.; Huang, M.; Jiang, H. Wettable Photothermal Hollow Fibers Arrays for Efficient Solar-Driven Desalination under Omnidirectional Illumination without Salt Precipitation. *Mater. Today Energy* **2020**, *16*, 100391. https://doi.org/10.1016/j.mtener.2020.100391.
- 705 (69) Wang, Y.; Wu, X.; Shao, B.; Yang, X.; Owens, G.; Xu, H. Boosting Solar Steam Generation 706 by Structure Enhanced Energy Management. *Sci. Bull.* **2020**, 65(16), 1380–1388. 707 https://doi.org/10.1016/j.scib.2020.04.036.
- 708 Wang, Y.; Wu, X.; Gao, T.; Lu, Y.; Yang, X.; Chen, G. Y.; Owens, G.; Xu, H. Same Materials, 709 Bigger Output: A Reversibly Transformable 2D–3D Photothermal Evaporator for Highly 710 Efficient Solar Steam Generation. Nano Energy 2021. 105477. 79. 711 https://doi.org/10.1016/j.nanoen.2020.105477.
- 712 (71) Li, S.; He, Y.; Wang, Y.; Liao, D.; Liu, H.; Zhou, L.; Wei, C.; Yu, C.; Chen, Y. Simple Hierarchical Interface Design Strategy for Accelerating Solar Evaporation. *Macromol. Mater. Eng.* **2020**, 2000640. https://doi.org/10.1002/mame.202000640.
- 715 Chen, Z.; Li, Q.; Chen, X. Porous Graphene/Polyimide Membrane with a Three-(72)716 Dimensional Architecture for Rapid and Efficient Solar Desalination via Interfacial 717 Evaporation. ACS Sustain. Chem. Eng. 2020, (36),13850-13858. 718 https://doi.org/10.1021/acssuschemeng.0c05306.